UC Davis
UC Davis Previously Published Works

Title

Saharan dust and the African easterly jet–African easterly wave system: Structure, location and energetics

Permalink

Journal

ISSN

Authors

Bercos-Hickey, Emily
Nathan, Terrence R
Chen, Shu-Hua

Publication Date

DOI

Peer reviewed

Saharan dust and the African easterly jet–African easterly wave system: Structure, location and energetics

Emily Bercos-Hickey,* Terrence R. Nathan and Shu-Hua Chen

Atmospheric Science Program, Department of Land, Air, and Water Resources, University of California, Davis, CA, USA

*Correspondence to: E. Bercos-Hickey, Atmospheric Science Program, Department of Land, Air, and Water Resources, University of California, One Shields Avenue, Davis, CA 95616-8627, USA. E-mail: ebercosh@ucdavis.edu

Abstract

The radiative effects of Saharan mineral dust (SMD) aerosols on the structure, location and energetics of the African easterly jet–African easterly wave (AEJ-AEW) system are examined for July–September 2006. Experiments are conducted with and without SMD using the Weather Research and Forecasting (WRF) model, which is radiatively coupled to an interactive dust model. The SMD-modified heating field shifts the AEJ northward, upward and westward, and enhances its zonal asymmetry. These SMD-induced changes to the AEJ are manifest in the AEWs: the northern and southern tracks of the AEWs shift northward (like the AEJ); and the zonal-scale of the AEWs expands and their westward propagation increases. The SMD also strengthens the energetics of the AEJ-AEW system. The domain and temporally averaged baroclinic energy conversion, which is an order of magnitude larger than the barotropic conversion, increases by a factor of 2.5. The eddy kinetic energy and generation of available potential energy increase by factors of 1.5 and 2.7, respectively. The implications of an SMD-modified AEJ-AEW system for West African precipitation and tropical cyclogenesis in the eastern Atlantic Ocean are discussed.

Key Words: African easterly jet; African easterly waves; Saharan dust

1 Introduction

The African easterly jet (AEJ) and African easterly waves (AEWs) are signature features of the summertime circulation over North Africa (Burpee, 1972; Reed *et al*., 1988; Thorncroft and Blackburn, 1999). Together the AEJ and AEWs constitute a system that affects not only regional weather (Reed *et al*., 1977), but also the weather over the eastern Atlantic Ocean, and even as far as the Caribbean (Riehl, 1954; Frank, 1970). Studies show, for example, that the AEJ-AEW system influences convection and rainfall over West Africa (Carlson, 1969a, 1969b; Reed *et al*., 1977), while more than half of the tropical cyclones that have been observed to develop over the eastern Atlantic Ocean from 1967 to 1991 had AEW origins (Landsea, 1993).

The AEJ-AEW system itself has been shown to be influenced by several forcings operating over North Africa, including the seasonal cycle (Thorncroft and Hodges, 2001), deep moist convection (Thorncroft and Blackburn, 1999; Cornforth *et al*., 2009), and, the focus of this study, synoptic-scale plumes of

Saharan mineral dust (SMD) aerosols (Grogan *et al*., 2016, 2017; Nathan *et al*., 2017).

The Sahara Desert is the most significant source of mineral dust in the atmosphere (Tanaka and Chiba, 2006). Several mechanisms loft SMD into the atmosphere. The mechanisms include mobilization by nocturnal low-level jets (Chen *et al*., 2008; Fiedler *et al*., 2013), formation of haboobs from the cold near-surface outflow of moist convection (Knippertz and Todd, 2012), and lofting by dry convection during the daytime in summer, which is associated with enhanced vertical winds and turbulence near the surface (Engelstaedter and Washington, 2007). AEWs also contribute to the emission and transport of SMD (Jones *et al*., 2004; Knippertz and Todd, 2010). Once formed, the synoptic-scale plumes of SMD are often carried westward toward the Atlantic within a layer of warm, dry air that is elevated by an encroaching cool, moist marine boundary layer to form the Saharan air layer (SAL). The plumes often continue to migrate westward, reaching the United States, Caribbean, and even South America (Engelstaedter *et al*., 2006). As the plumes propagate westward from North Africa, they absorb, scatter and emit radiation to affect the energy budget of the atmosphere and the surface (Zhu *et al*., 2007), which modifies the atmospheric circulation (Chen *et al*., 2010).

Despite the complexity of the AEJ-AEW system, progress has been made on understanding how SMD affects its structure and evolution. Reanalysis studies (Tompkins *et al*., 2005; Wilcox *et al*., 2010) and numerical modelling studies (Reale *et al*., 2011) both show that the location of the AEJ is in closer agreement with observations when SMD feedbacks are accounted for. For example, Tompkins *et al*. (2005) showed that an updated aerosol climatology improved 5-day reanalysis forecasts of the AEJ. Wilcox *et al*. (2010) used nine years of satellite and reanalysis data to show that outbreaks of SMD shift the AEJ northward. And Reale *et al*. (2011) used the NASA GEOS-5 model to run 5-day forecasts and showed that the inclusion of aerosols in the model changed the temperature field, causing the AEJ to shift northward and upward in the direction of the dust plume.

Studies examining the effects of SMD on AEWs have produced conflicting results. Some studies have shown that SMD weakens AEWs (Karyampudi and Carlson, 1988; Reale *et al*., 2009; Jury and Santiago, 2010), whereas others have shown that it strengthens AEWs (Jones *et al*., 2004; Ma *et al*., 2012; Grogan *et al*., 2016). The modelling study by Reale *et al*. (2009) and the statistical study by Jury and Santiago (2010) both find that as dust increases in the SAL, the dust-radiative heating causes mid-level temperatures to increase relative to those below. The result is an increase in the static stability over the Atlantic Ocean, which creates less favourable conditions for the strengthening of AEWs.

In contrast, Jones *et al*. (2004) used reanalysis data and dust from a global transport model and found that SMD enhances AEWs over the Atlantic Ocean

through dust-induced warming in the lower troposphere, which reduces static stability. Ma *et al*. (2012) used the Weather Research and Forecasting (WRF) model with a prescribed dust layer and found, similar to Jones *et al*. (2004), a reduction in static stability. Ma *et al*. (2012) found that the reduction in stability increased convection, which was correlated with an increase in eddy kinetic energy (EKE), resulting in the strengthening of most of the AEWs in the model.

The above studies attribute AEW growth or decay to SMD-induced changes in the static stability. Focusing on static stability alone, however, provides an incomplete picture. Indeed, as shown by Grogan *et al*. (2016, 2017) and Nathan *et al*. (2017), SMD can affect AEW growth via two additional feedback mechanisms. The mechanisms involve SMD-induced changes to (i) the eddy heating field and (ii) the zonal-mean heating field, which together change the eddy and zonal-mean portions of the circulation.

For example, using a linearized version of the WRF model coupled to an interactive dust model, Grogan *et al*. (2016) showed that for a realistic zonal-mean background wind that is *supercritical* with respect to the barotropic and baroclinic instability threshold, the SMD-induced changes to the eddy heating field strengthened the AEWs, i.e. the SMD increased the growth rates of the AEWs by ~5–20%.

Nathan *et al*. (2017) showed that SMD alone, through its eddy heating feedbacks, could destabilize AEW-like waves in zonal-mean background flows that are *subcritical* with respect to barotropic and baroclinic instability. Using Grogan *et al*.'s (2016) WRF-dust model, Nathan *et al*. (2017) showed that for a subcritical AEJ and a background SMD distribution that are consistent with observations, SMD destabilizes the AEWs and slows their westward propagation. Particularly striking was the fact that the SMD-induced growth rates could exceed those obtained in previous dust-free studies in which AEWs grow on supercritical AEJs.

Grogan *et al*. (2017) showed that the SMD eddy and zonal-mean heating fields together modify the AEW life cycles in the WRF-dust model. The SMD-modified life cycles are characterized by enhanced linear growth, weakened nonlinear stabilization, larger peak amplitude, and smaller long-time amplitude. SMD also enhances the Eliassen–Palm flux divergence and residual mean meridional circulation, which generally oppose each other throughout the AEW life cycle. And throughout the AEW life cycle, the SMD-modified AEJ is elevated and the peak winds are larger than without SMD.

Although the studies cited above have advanced understanding of the effects of SMD on the AEJ-AEW system, several unresolved issues remain. For example, although it has been shown that SMD can affect the meridional and vertical location of the AEJ (Tompkins *et al*., 2005; Wilcox *et al*., 2010; Reale *et al*., 2011; Grogan *et al*., 2017), it is unclear how SMD affects its zonal location. How do the SMD-induced changes to the location and shearing of the AEJ manifest in the location and strength of the energy conversions of

the AEJ-AEW system? And how might SMD affect the tracks, wavelengths, and propagation of AEWs? To address these questions, we focus on a single boreal summer over North Africa, the region where AEWs and plumes of SMD are born.

The article is organized as follows: section 2 describes the model and the methods of analysis. In section 3, the SMD distribution is described, followed by section 4 in which the temperature field and the AEJ are compared with and without the radiative effects of SMD. Section 5 focuses on the structure, location, strength and energetics of AEWs. A discussion of the wave–mean flow interaction pathways operating within the SMD-modified AEJ-AEW system is presented in section 6, and the conclusions are presented in section 7.

2 Model, experiments and analysis

2.1 *Model*

The radiative effects of SMD on the AEJ-AEW system are examined using the WRF model, which is radiatively coupled to an interactive dust model (Chen *et al*., 2010, 2015). The WRF-dust model is a modified version of WRF 3.7.1, which is a nonhydrostatic, compressible model that uses a third-order Runge–Kutta scheme in time, the Arakawa C grid, high-order advection schemes, and terrain-following mass coordinates.

In the WRF-dust model, the evolution of SMD is governed by a dust continuity equation, wherein the rate of change of the mass coupled dust mass mixing ratio is due to the flux divergence of SMD, mixing of SMD by boundary-layer turbulence and subgrid-scale convection, sedimentation, scavenging, dry and wet deposition, and surface emission. The surface emission occurs when the vegetation type is barren, the soil volumetric moisture is less than 0.2, and the 10 m wind speed exceeds a threshold of 6 m s^{-1} (Tegen and Fung, 1994; Chen *et al*., 2010). The radiative forcing due to SMD is incorporated into the WRF-dust model through the thermodynamic equation. The SMD-radiative effects are included using the short-wave radiation scheme of the Rapid Radiative Transfer Model for Global Climate Models (Iacono *et al*., 2008).

The WRF-dust model uses five SMD particle sizes to represent the spectrum of mineral dust sizes over North Africa. The division of SMD into five bins results in a four-dimensional variable consisting of the spatial directions *x*, *y* and *z*, and bin size. The aerosol properties of the different types of SMD are calculated using the Optical Properties of Aerosols and Clouds (OPAC) software package (Hess *et al*., 1998). The SMD optical properties include the asymmetry parameter, single-scatter albedo, and extinction coefficient, all as a function of wavelength and SMD particle size. Fourteen wavelength bands are included in the short-wave, varying from 0.25 to 7.9 microns. Nucleation, accumulation and coagulation are the only three modes of SMD in OPAC. The five bins of SMD are therefore combined into the three mass-

conserving modes when calculating the optical properties. The coefficients of the optical properties are stored in look-up tables to be used in the radiation schemes of the WRF-dust model.

2.2 *Experiments and analysis*

Experiments were conducted with and without SMD. The first experiment, DUST-ON, includes SMD transport and radiative effects, whereas the second experiment, DUST-OFF, excludes SMD radiative effects. Both experiments were conducted for a single summer spanning July through September 2006. National Aeronautics and Space Administration (NASA) Moderate Resolution Imaging Spectroradiometer (MODIS) Aqua and Terra satellite aerosol optical depth (AOD) data are available for this season, which will ease verification of the model results.

European Centre for Medium-range Weather Forecasts (ECMWF) reanalysis interim data were used in both experiments to generate the boundary and initial conditions for the WRF-dust model. The two-moment microphysics scheme (Cheng *et al*., 2010), the Medium Range Forecast (MRF) boundary layer parametrization (Hong and Pan, 1996), and the Kain–Fritsch (KF) cumulus parametrization (Kain, 2004) were used for both experiments and are all equipped to handle SMD. Model output was generated every 6 h and two domains were used with 36 km outer and 12 km inner domain grid spacing. We used four-dimensional data assimilation (FDDA) to nudge the outer domain model fields to the reanalysis data. The outer domain has 38 grid points in the vertical and spans the area 80°W–55°E and 30°S–60°N. The inner domain, which is used for our analysis, has 38 grid points in the vertical and spans the area 60°W–35°E and 5°S–45°N, which encompasses the SMD-modified AEJ-AEW system.

The model-generated data are time-averaged for the 2006 summer season, except for the calculations involving phase differences. For the construction of the vertical cross-sections to be presented later, zonal averages are taken between 30°W and 0°. This longitudinal range focuses on North Africa and the eastern Atlantic Ocean and ensures that the complete zonal scales (wavelengths) of the AEWs are captured. To isolate the AEWs, the perturbations in wind, temperature, and dust diabatic heating rate are temporally and spatially filtered. The temporal filtering spans 3–5 days and the spatial filtering spans 2000–4000 km (zonal wavelengths). The filtered values are used in the AEW track analysis and in the covariance calculations.

3 Dust concentration and structure

The concentration and distribution of SMD over North Africa has been examined using AOD as a proxy for column dust amount (Slingo *et al*., 2006; Ma *et al*., 2012; Grogan *et al*., 2016). The AOD over North Africa can vary from values as low as ~0.2 to as much as ~4.0 during severe dust emission (Slingo *et al*., 2006; Kocha *et al*., 2012).

Figure 1(a) shows the model-generated AOD. The maximum AOD is ~1.3 at (20.2°N, 15.7°W), which falls within ~18–22°N, the latitude belt that contains hot spots, regions of large SMD emissions that occur over the Bodélé Depression in Chad, and over parts of Mauritania, Mali and Algeria (Engelstaedter and Washington, 2007). The regions where the AOD exceeds one include the Western Sahara and the Bodélé Depression, the main source regions of SMD. The SMD plume between the Western Sahara and the Bodélé Depression occupies a broad area, spanning 20°W–20°E and 15°N–25°N. This region is about the same zonal scale as an AEW; it also coincides with the region occupied by the AEJ and pronounced AEW activity (Reed *et al*., 1988; Pytharoulis and Thorncroft, 1999).
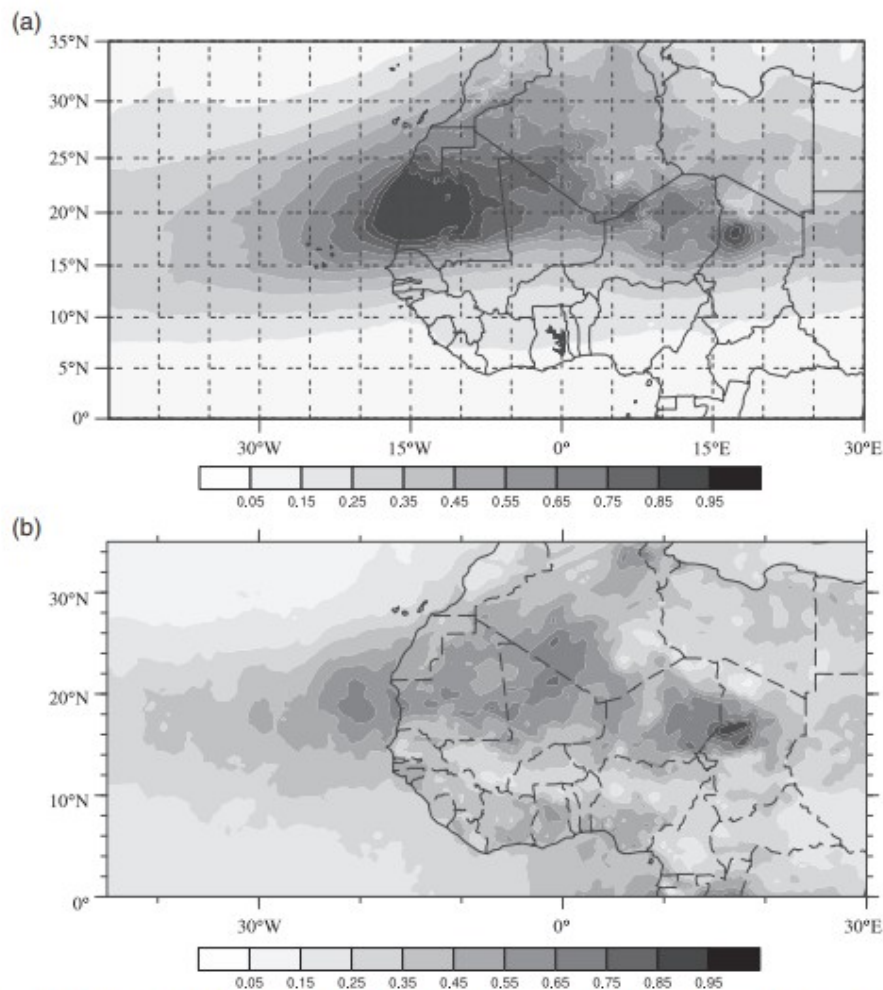
Figure 1. July–September 2006 time-averaged AOD from (a) DUST-ON, and from (b) the NASA MODIS Aqua and Terra satellites at 550 nm.

Figure 1(b) shows the fused NASA Aqua and Terra MODIS AOD over North Africa. Comparison of Figures 1(a) and (b) shows that the modelled region of AOD > 1.0 is in the same region as the largest AOD obtained from the satellite data, although the model AOD is on average ~15% greater. The smaller satellite-derived AOD measurements may not be too surprising, since such measurements are often underestimated over deserts (Xie *et al*., 2011;

Banks *et al.*, 2013). For example, over the Western Sahara, MODIS underestimated the AOD by 65% during a dust-storm in June 2011 (Banks *et al.*, 2013). Nevertheless, despite the differences between the satellite data and the model data, their general agreement lends confidence in the ability of the WRF-dust model to replicate the key features of the SMD-modified AEJ-AEW system.

Figure 2 shows the vertical cross-section of the model-produced SMD concentrations, summed over the five SMD particle sizes. The plume is maximized at the surface near ~21°N, above which it monotonically decreases with height. Sharp, positive meridional and vertical gradients of SMD are between 15 and 20°N and between the surface and 500 hPa, respectively. The importance of the spatial gradients of SMD to the growth of AEWs has been underscored in Grogan *et al.* (2016) and Nathan *et al.* (2017), who found that the effects of SMD on the linear dynamics of AEWs are strongest where the gradients are largest. Grogan *et al.* (2016) found, for example, an SMD-induced increase in the baroclinic and barotropic energy conversions and in the generation of eddy available potential energy (APE) between 15 and 20°N, the location where the maximum meridional gradient of SMD coincides with the critical surface. The location of the maximum meridional SMD gradient in this study matches that of Grogan *et al.* (2016), despite their use of a prescribed basic state SMD distribution and the neglect of most of the physical processes included in the version of the WRF-dust model used here (e.g. boundary-layer mixing, dry and wet SMD deposition, and SMD surface emission).
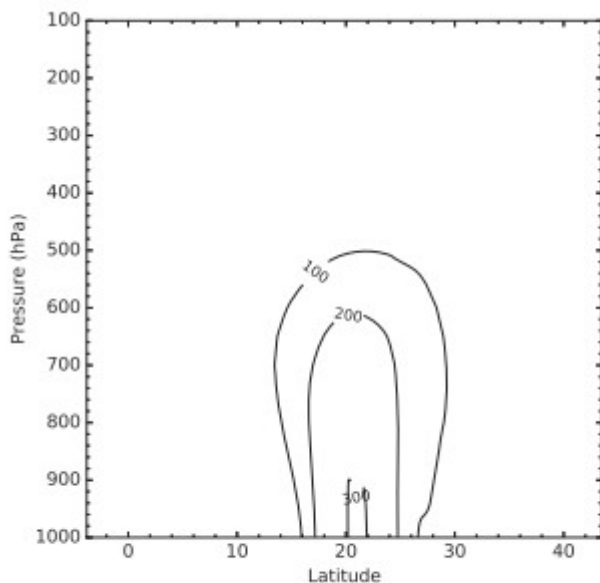

Figure 2. Vertical cross-section of dust concentration in µg kg⁻¹. Time averaged over July–September 2006 and zonally averaged between 30°W and 0°.

4 Temperature and AEJ structures

We begin by validating the WRF-dust model results using ECMWF reanalysis data for temperature and zonal wind. Because the ECMWF reanalysis data includes the effects of SMD through the assimilation of temperature observations, which include dust radiative effects, the expectation is that DUST-ON will align more closely with the reanalysis data.

Figure 3 shows the time and zonally averaged temperature (Figure 3(a)) and zonal wind (Figure 3(b)) from the ECMWF reanalysis data. The meridional temperature gradient is positive from 0 to 22°N and from the surface to ~600 hPa, consistent with cooler temperatures in the Sahelian region and warmer temperatures in the Sahara. The largest positive meridional temperature gradient is at ~15°N, which coincides with the location of the AEJ core, seen in the zonal wind field at 15°N and 600 hPa. The relationship between the meridional temperature gradient and the AEJ is consistent with thermal wind balance.
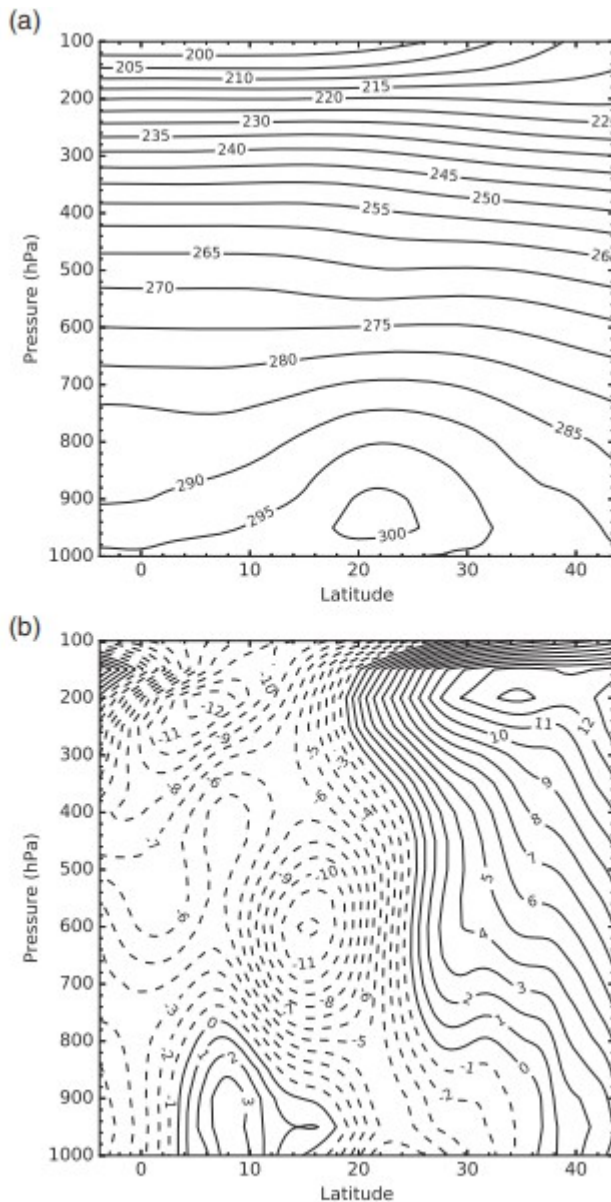
(a)

(b)

Figure 3. Vertical cross-sections from ECMWF reanalysis data of (a) temperature in Kelvins, and (b) zonal wind in ms^{-1}. Plots are time-averaged over July–September 2006 and zonally averaged between 30°W and 0°.

Figure 4 shows the time and zonally averaged temperature difference between the ECMWF reanalysis data and DUST-ON (Figure 4(a)) and DUST-OFF (Figure 4(b)), and the temperature difference between DUST-ON and DUST-OFF (Figure 4(c)). A comparison of Figures 4(a) and (b) shows that with SMD the temperature field is in closer alignment with the reanalysis data. For example, at and above the AEJ level, DUST-ON temperatures are up to 1.4 K cooler than the reanalysis data, while DUST-OFF temperatures are up to 1.8 K cooler. Near the surface, DUST-ON temperatures are up to 1.8 K warmer, while DUST-OFF temperatures are up to 2.2 K warmer. Because the temperature and AEJ are connected through thermal wind balance, it is

important that the temperature be accurately represented in the model. With SMD, the model-produced temperature field is closer to the reanalysis data and would therefore be expected to produce a more accurate AEJ.
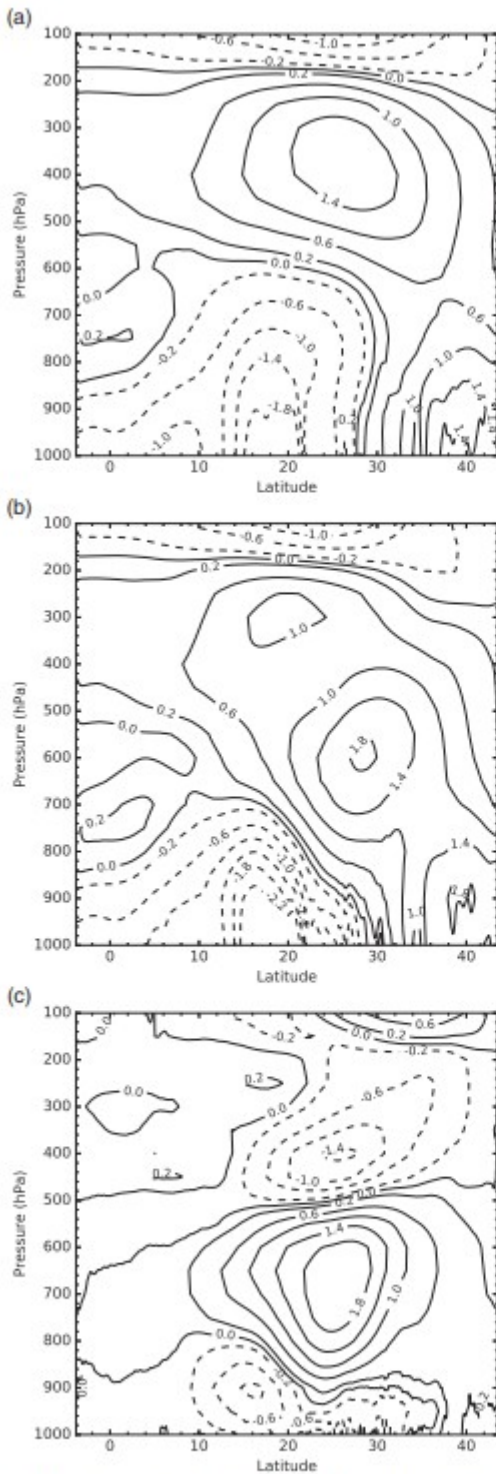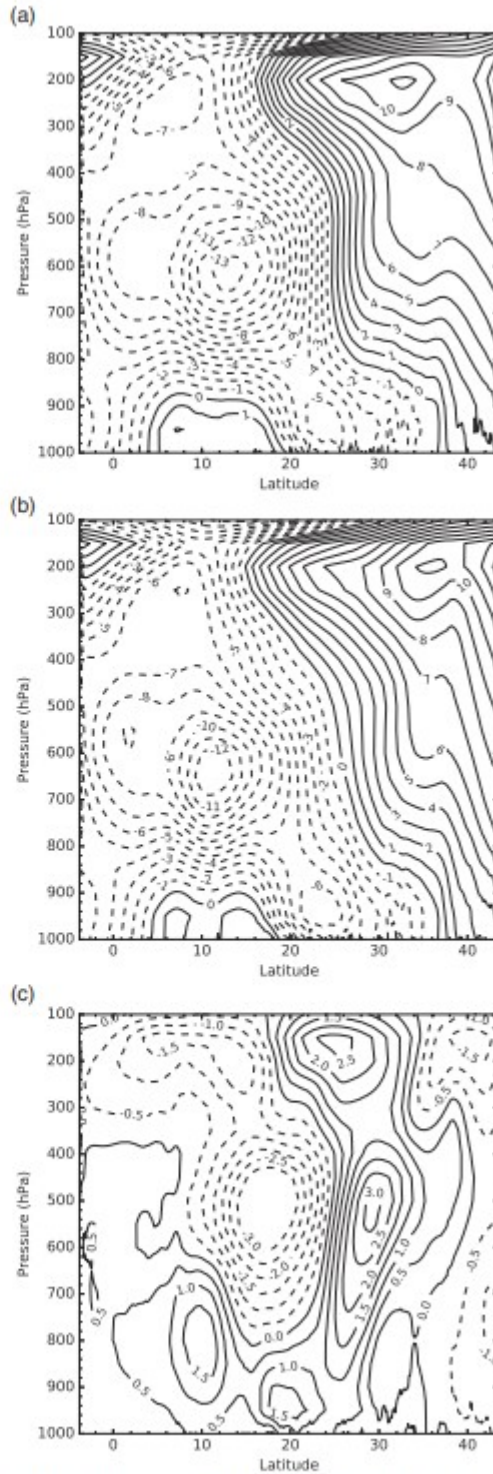

Figure 4. Vertical cross-sections of temperature in Kelvins, time averaged over July–September 2006 and zonally averaged between 30°W and 0°, for the ECMWF data minus (a) DUST-ON, (b) DUST-OFF, and (c) DUST-ON minus DUST-OFF. Solid and dashed contours indicate positive and negative values, respectively.

Figure 5. Vertical cross-sections of the zonal wind in m s⁻¹, time-averaged over July–September 2006 and zonally averaged between 30°W and 0°, for (a) DUST-ON, (b) DUST-OFF and (c) the difference between DUST-ON and DUST-OFF. Solid and dashed contours indicate westerly and easterly values, respectively.

Figure 4(c) shows that SMD warms the 900–600 hPa layer by ~0–2.0 K and cools the layer near the surface by ~0–1.0 K. This SMD-induced temperature change, which is consistent with previous studies (Wong *et al.*, 2009; Reale *et al.*, 2011), has two important consequences. First, the low-level cooling and the jet-level warming produce a more stable stratification below 600 hPa, which has been associated with weaker AEWs (Reale *et al.*, 2009; Jury and Santiago, 2010). Second, the SMD-induced temperature change affects the vertical shear and thus the AEJ via thermal wind balance (Chen *et al.*, 2010), which can alter the barotropic and baroclinic energy conversions to affect AEW growth, an important point that we examine in section 5.

Figure 5 shows the effects of SMD on the latitude and height of the zonally averaged AEJ. With SMD, the AEJ axis is at ~600 hPa and ~13.5°N, with a peak wind speed of -13.6 m s^{-1} (Figure 5(a)). Without SMD, the AEJ is lower (~650 hPa), farther south (~11°N), and weaker (peak wind speed of -12.9 m s^{-1}; see Figure 5(b)). Comparison of Figures 5(a) and (b) shows that SMD shifts the AEJ upward by ~50 hPa and northward by ~3°, bringing the AEJ core in closer alignment with the ECMWF AEJ located at 15°N and 600 hPa (Figure 3(b)). The SMD-induced increase in the peak wind speed is consistent with Grogan *et al.* (2017), who used a simplified version of the WRF-dust model. The improved location of the AEJ core with SMD lends confidence in the accuracy of the WRF-dust model in replicating the key circulation features over North Africa.

Figure 5(c) shows that at ~17°N and ~550 hPa, there is a ~1–3 m s^{-1} (negative) zonal wind difference between DUST-ON and DUST-OFF. This wind difference is consistent with the ~0–2.0 K (positive) temperature difference between DUST-ON and DUST-OFF shown in Figure 4(c). These SMD-induced differences correspond to northward and upward shifts in the zonal wind and its shear, and the temperature field and its gradient.

Figure 6 shows horizontal cross-sections of the zonal wind at the jet core for both experiments. We use the half-width of the AEJ kinetic energy, which corresponds to zonal wind values <-9 m s^{-1}, to define the zonal extent of the jet core. The white circles in Figure 6 show the locations of the maximum easterly zonal wind speed. With SMD, the zonal wind is maximized at 13.7°N and 21.7°W (Figure 6(a)); without SMD, the zonal wind is maximized at 10.0°N and 12.5°W (Figure 6(b)). Consistent with previous studies (Tompkins *et al*., 2005; Wilcox *et al*., 2010; Reale *et al*., 2011), the SMD-induced heating shifts the maximum wind speed north by ~3°. The previous studies, however, did not examine the effects of SMD on the longitudinal position of the AEJ core, which we find shifts west by ~9° (~1000 km).
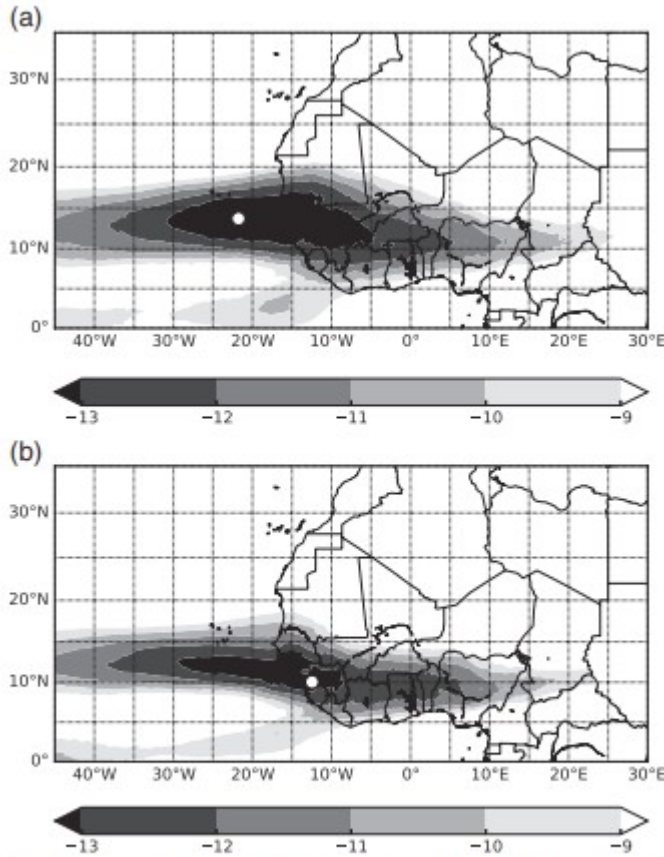
Figure 6. July–September 2006 time-averaged zonal wind in m s^{-1} for (a) DUST-ON at 600 hPa and (b) DUST-OFF at 650 hPa. White circles indicate the location of the maximum wind speed.

Figure 6 also shows the SMD-induced changes in the horizontal structure of the AEJ. SMD increases the meridional shear of the zonal wind by ~70% north of the jet maximum and ~30% south of the jet maximum. West of the jet maximum, the meridional width of the AEJ is on average ~20% wider with SMD (Figure 6(a)), and to the east, the width is on average ~30% wider with SMD (Figure 6(b)). SMD also increases the zonal shear of the zonal wind; with SMD, the zonal shear is ~110% larger west of the jet maximum.

Figure 7 shows the zonal and meridional extent of the AEJ core for both experiments. The spatial extents of the AEJ were calculated using the location of the maximum zonal wind speeds at 600 hPa for DUST-ON and 650 hPa for DUST-OFF. In Figure 7(a), a meridional average was taken between 5° north and south of the maximum wind speed; the vertical lines denote the longitudinal locations of the peak wind speed for DUST-ON (dashed) and DUST-OFF (solid). In Figure 7(b), the zonal average was taken between 5° east and west of the maximum wind speed.
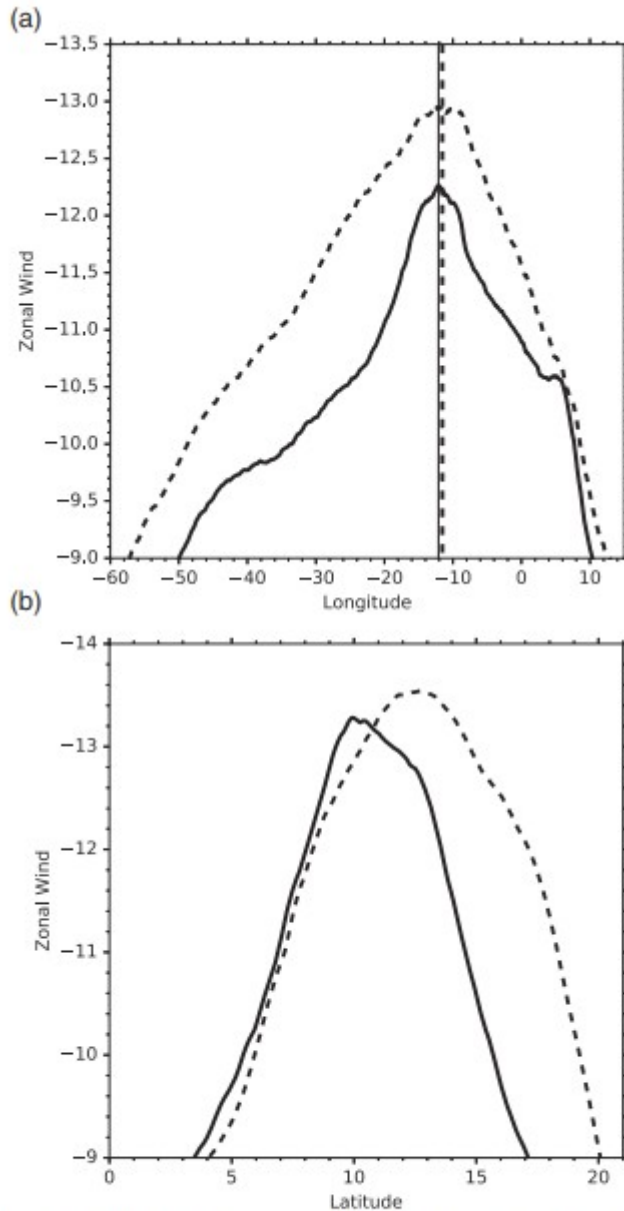
Figure 7. Zonal wind profile in m s^{-1} for DUST-ON (dashed) and DUST-OFF (solid), which are (a) meridionally averaged and (b) zonally averaged. The profiles were time-averaged and chosen at the pressure level of the maximum zonal wind speed. The vertical lines in (a) indicate the longitude of the AEJ cores.

Figure 7(a) shows that SMD affects the zonal asymmetry of the AEJ. With SMD, the zonal extent of the AEJ on the downstream side of the jet core is on average ~75% wider than on the upstream side. Without SMD, however, the zonal extent of the AEJ on the downstream side is on average only ~30% wider than the upstream side. This zonal asymmetry in the AEJ is important as the zonal extent of the AEJ largely determines the zonal extent of the AEWs (Hall *et al*., 2006). Figure 7(b) shows that SMD has little effect on the meridional asymmetry of the AEJ, but shifts it ~3° northward, which, as expected, agrees with Figures 5 and 6.

5 African easterly waves

5.1 *AEW tracks, wavelengths, and phase speeds*

The location of the AEW tracks averaged for July–September 2006 was calculated using the filtered EKE. Figure 8 shows, consistent with previous studies (Reed *et al*., 1988; Pytharoulis and Thorncroft, 1999), distinct northern and southern tracks for both experiments. Figures 8(a) and (b) are at 900 hPa and Figures 8(c) and (d) are at 700 hPa, which are the primary pressure levels associated with the northern and southern tracks (Reed *et al*., 1988). For illustrative purposes, solid lines are shown over the EKE contours to indicate the main track locations. The lengths of the tracks were chosen to match the lengths of their respective AEJ axes, which are also shown (dashed lines).
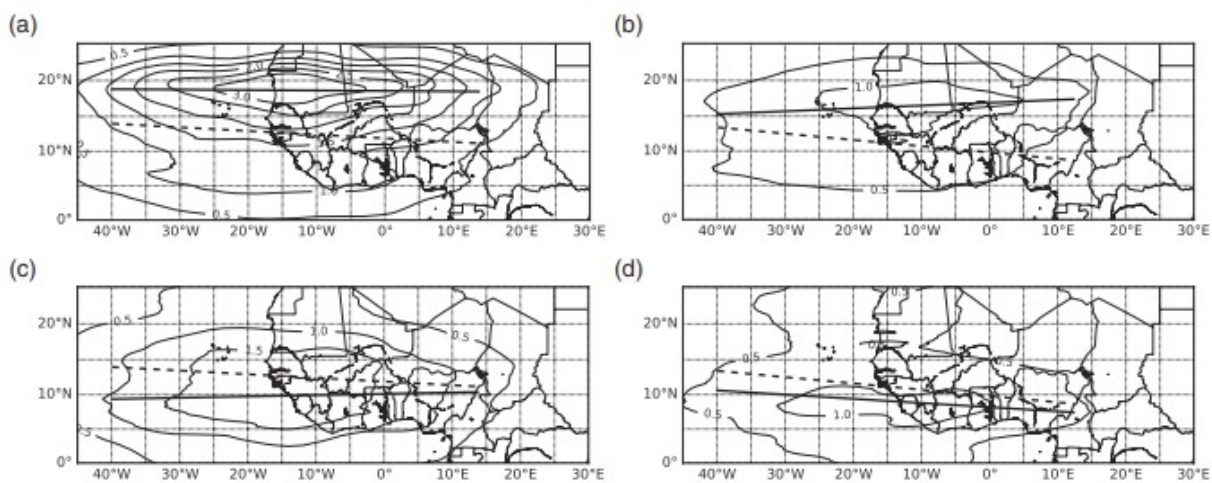

Figure 8. Filtered eddy kinetic energy in m² s⁻² at 900 hPa for (a) DUST-ON and (b) DUST-OFF, and at 700 hPa for (c) DUST-ON and (d) DUST-OFF. Also shown are the AEJ axes (thick dashed) and the main AEW tracks (thick solid).

Figure 8 shows that including SMD shifts the AEJ axis north by ~3°, as also seen in section 4. Because the AEWs draw on energy from the AEJ and are thus largely tethered to it, shifts in the AEJ will cause shifts in the AEW tracks. Indeed, Figure 8 shows that the northern and southern AEW tracks shift north by ~2.0° and ~3.0°, respectively. The SMD-modified track locations agree with previous reanalysis studies (Reed *et al*., 1988; Thorncroft and Hodges, 2001).

Figure 8 also shows that for both tracks, the EKE with SMD is a factor of 1.5–2 greater than without SMD. The largest EKE is located in the SMD-modified northern track where the SMD meridional gradients are largest.

To determine the effects of SMD on the zonal wavelengths and phase speeds of the AEWs, we follow Reed *et al*. (1988) and calculate the average phase difference between the July–September 2006 meridional wind time series at 15°W and neighbouring longitudes. We choose 15°W because it is near the longitude of the jet core and because it was used by Reed *et al*. (1988). The meridional wind is taken at two latitudes and pressures, 17°N at 900 hPa and

10°N at 700 hPa, to correspond with the northern and southern AEW tracks seen in Figure 8. We anticipate, due to the zonal variations of the AEJ, that the AEWs will respond in spatial scale and speed differently upstream and downstream of the jet core. Previous research has indeed shown that AEWs are spatially modulated as they propagate westward. For example, using two months of reanalysis data from 1985, Reed *et al*. (1988) found that the AEW wavelengths expanded from 2500 to 2700 km (~8%) as they propagated westward. In contrast, Kiladis *et al*. (2006) found using 15 years of reanalysis data that the zonal wavelengths contracted by ~30% as they propagated westward. The difference between Reed *et al*. (1988) and Kiladis *et al*. (2006) may be due to their use of different datasets and time periods.

To determine the effects of SMD on the zonal wavelengths and phase speeds of AEWs, we first consider the northern track. Upstream of the AEJ core, the zonal wavelength is ~2800 km with SMD, which, because the period of AEWs is approximately constant, yields a westward phase speed of ~8.1 m s^{-1}. (Because the AEJ is time invariant (a consequence of the time-averaging), the AEW periods (frequencies) will be approximately constant, a fact that can be demonstrated from kinematic wave theory (see, for example, Pedlosky (2003), his section 2).) Downstream of the AEJ core, however, the zonal wavelength and phase speed are ~3400 km and ~9.8 m s^{-1} with SMD. Without SMD, the zonal wavelength and phase speed are ~2800 km and ~8.1 m s^{-1} upstream, and ~3200 km and ~9.3 m s^{-1} downstream. The differences in wavelengths for the northern track AEWs equate to a downstream expansion of ~20% with SMD, and ~15% without SMD. For the southern track AEWs, the zonal expansion is ~15% with SMD, and ~10% without SMD. These results qualitatively agree with Reed *et al*. (1988). All of the wavelengths span ~2000–4000 km, consistent with observed AEWs (Burpee, 1972). The zonal expansion of the AEWs in the northern and southern tracks is largely a result of the zonal asymmetry of the AEJ (Figure 7(a)). Kiladis *et al*. (2006) suggest that zonal changes of the AEWs are due to 'a dynamical effect rather than one due to convective coupling'. Here, the longer zonal extent of the AEJ on the downstream side of the AEJ core manifests in the zonal expansion of the AEWs.

5.2 *Energetics*

Several studies have examined the energetics of the AEJ-AEW system without addressing the radiative effects of SMD (Burpee, 1972; Reed *et al*., 1988; Pytharoulis and Thorncroft, 1999; Hsieh and Cook, 2007). The studies show that the baroclinic energy conversion is greater north of the AEJ at lower levels and that the barotropic energy conversion is greater south of the AEJ at jet level (Pytharoulis and Thorncroft, 1999; Hsieh and Cook, 2007). The EKE has been shown to follow a similar pattern, with larger values north of the AEJ at lower levels and south of the AEJ at jet level (Pytharoulis and Thorncroft, 1999; Hsieh and Cook, 2007). To determine how the dust-radiative heating affects the AEJ-AEW system, we calculate the SMD-modified diabatic generation of eddy APE, G_E, the baroclinic and barotropic energy

conversions, C_{pk} and C_k, and the EKE, K_E, using the domain-averaged expressions presented in Hsieh and Cook (2007):

$$G_E = \int_{Y_1}^{Y_2} \int_{P_1}^{P_2} G_E^* g^{-1} dp\, dy, \qquad (1a)$$

$$C_{pk} = \int_{Y_1}^{Y_2} \int_{P_1}^{P_2} C_{pk}^* g^{-1} dp\, dy, \qquad (1b)$$

$$C_k = \int_{Y_1}^{Y_2} \int_{P_1}^{P_2} C_k^* g^{-1} dp\, dy, \qquad (1c)$$

$$K_E = \int_{Y_1}^{Y_2} \int_{P_1}^{P_2} K_E^* g^{-1} dp\, dy, \qquad (1d)$$

where

$$G_E^* = \frac{[T'Q']}{\overline{\sigma} c_p}, \qquad (2a)$$

$$C_{pk}^* = -\frac{R}{p} [\omega'T'], \qquad (2b)$$

$$C_k^* = -[u'v']\frac{\partial [u]}{\partial y} - [u'\omega']\frac{\partial [u]}{\partial p} - [v'^2]\frac{\partial [v]}{\partial y} - [v'\omega']\frac{\partial [v]}{\partial p}, \qquad (2c)$$

$$K_E^* = \frac{[u'^2 + v'^2]}{2}. \qquad (2d)$$

In Eqs (1)-(1) and (2)-(2), u and v are the zonal and meridional winds; $\omega = dp/dt$ is the vertical motion; p is the pressure; T is the temperature; Q is the diabatic heating rate per unit mass due to radiative effects; g is the gravitational acceleration; C_p is the specific heat capacity at constant pressure; R is the gas constant for dry air; and $\overline{\sigma} = c_p^{-1} \overline{[T]} - pR^{-1} \partial \overline{[T]}/\partial p$ is the mean static stability. The notation [ ] denotes a zonal average, $\overline{[\ ]}$ denotes a meridional average of the zonal mean, and primes denote deviations from the zonal mean.

Previous studies of the energetics of the AEJ-AEW system that have not considered SMD have used two approaches. One approach calculates the domain-averaged energetics based on Eq. (1)-(1) (Hall *et al.*, 2006; Hsieh and Cook, 2007), while the other approach infers the energetics based solely on the calculation of the eddy covariances appearing in Eq. (2)-(2) (Reed *et al.*, 1988; Pytharoulis and Thorncroft, 1999). In this study, the second approach would provide an incomplete picture of the SMD-modified

energetics because, as we showed in section 4, SMD affects the zonal-mean wind and temperature fields, which are omitted in the eddy covariance approach. For this reason, the SMD-modified energetics of the AEJ-AEW system will be based on Eq. (1)-(1), where the integrands are given by Eq. (2)-(2). For the domain average, the integrals were evaluated from 1000 to 100 hPa to capture the entire column, the zonal average was taken between 30°W and 0°, and the meridional average was taken between 0° and 30°N to centre the AEJ within the domain. We have found that changes to the domain boundaries do not affect the conclusions presented below.

Table 1 shows that SMD increases all of the energetics terms. The SMD increases C_{pk} and C_k by factors of 2.5 and 22, respectively. Although the change in C_k is large, it is still an order of magnitude smaller than C_{pk}. The ratio C_{pk}/C_k is ~6 with SMD and ~50 without SMD. The fact that C_{pk} is significantly larger than C_k agrees with Hall *et al.* (2006) and Hsieh and Cook (2007). With SMD, G_E and K_E increase by factors of 2.7 and 1.5, respectively. The SMD-induced increase in the energetics terms was also found in the idealized linear stability analysis of Grogan *et al.* (2016).

Table 1. Baroclinic energy conversion, C_{pk}, barotropic energy conversion, C_k, diabatic generation of eddy available potential energy, G_E, in 10^{-2} W m^{-2}; eddy kinetic energy, K_E, in J m^{-2}.

	DUST-ON	DUST-OFF	$\frac{\text{DUST-ON}}{\text{DUST-OFF}}$
C_{pk}	6.4	2.60	2.5
C_k	1.1	−0.05	22.0
G_E	1.4	0.52	2.7
K_E	9739.5	6382.10	1.5

Figures 9-12 show the zonally and temporally averaged latitude–height cross-sections of the energy conversions from Eq. (2)-(2). Solid thick lines indicate the location of the AEJ maximum and dashed lines indicate the location of the maximum concentration of SMD. The area above 400 hPa is believed to be associated with the tropical easterly jet and not AEWs (Hsieh and Cook, 2007). We begin with an analysis of G_E^* and use this as a reference for the other energy conversions.
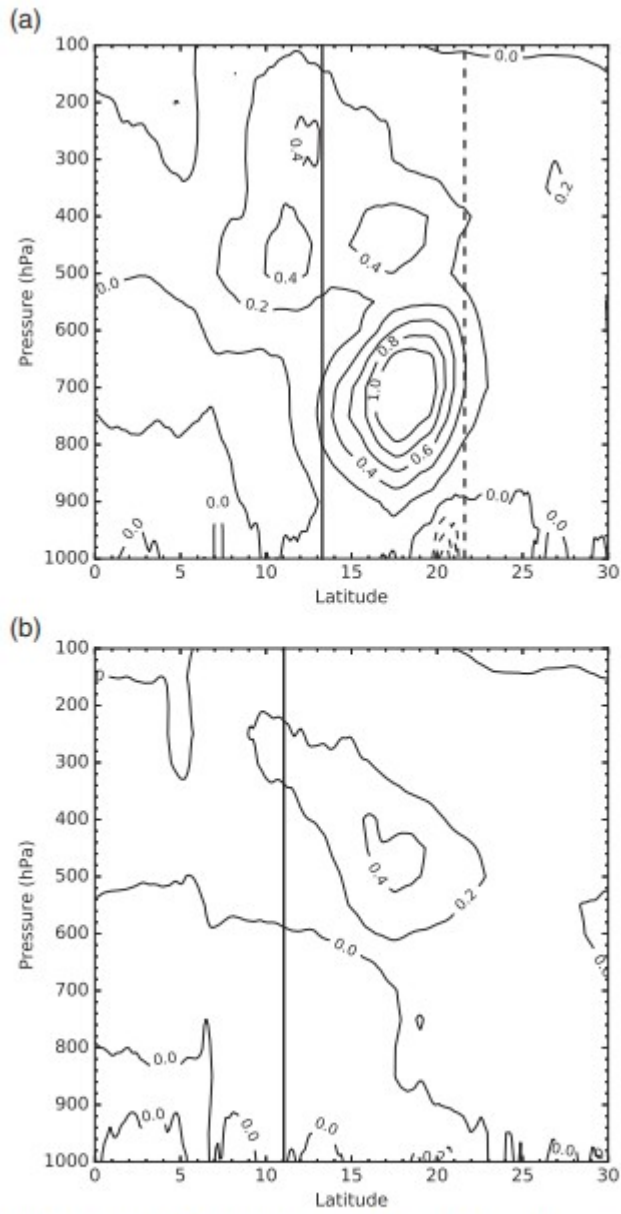
Figure 9. Generation of eddy available potential energy distribution, G_E^*, averaged between 30°W and 0° for (a) DUST-ON and (b) DUST-OFF (units: 10^{-5} m^2 s^{-3}). Solid vertical lines indicate the location of the AEJ maximum. Dashed vertical line indicates the location of the maximum SMD concentration.
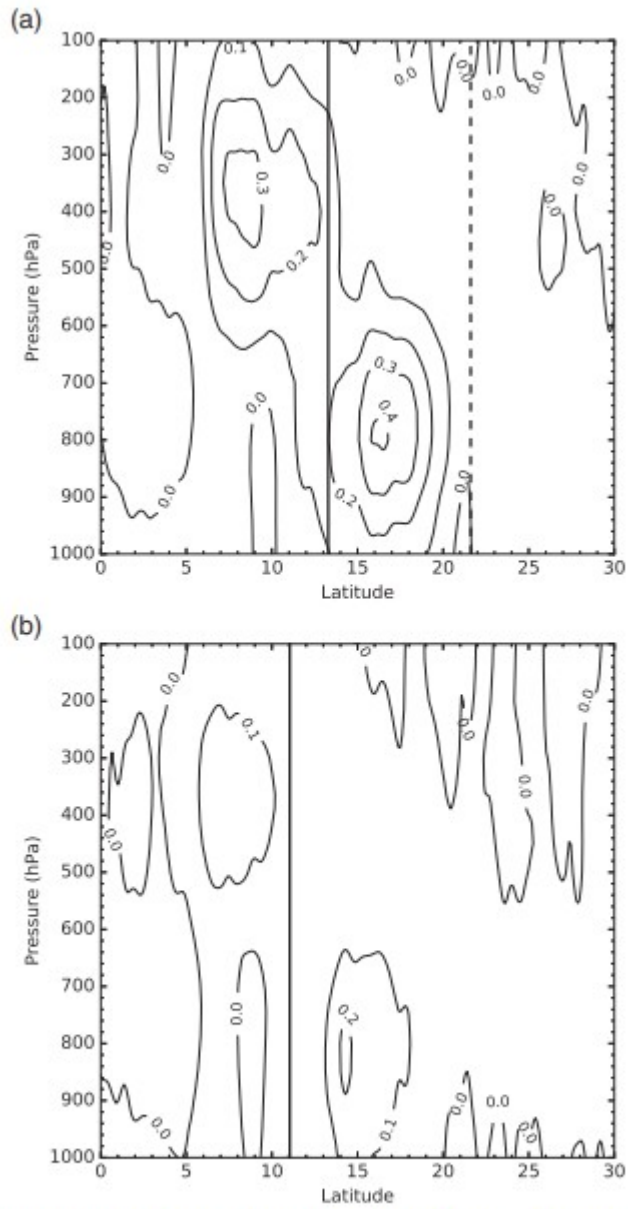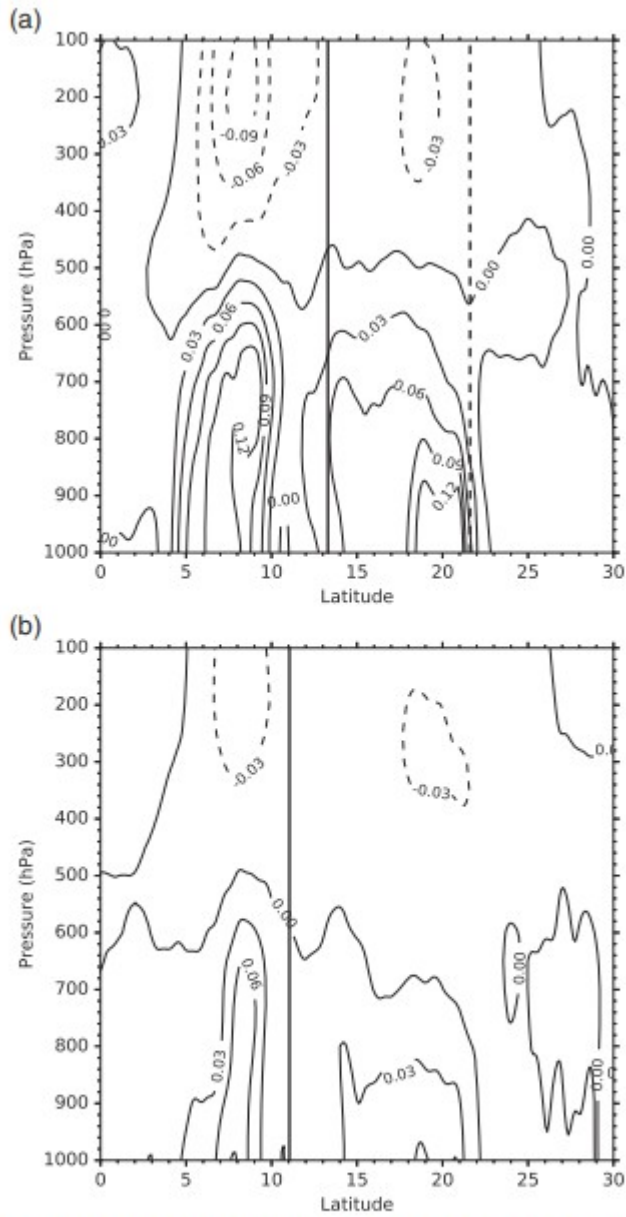
Figure 10. Baroclinic energy conversion distribution, $C_{p k}^{*}$, averaged between 30°W and 0° for (a) DUST-ON and (b) DUST-OFF (units: $10^{-4}\,\mathrm{m}^2\,\mathrm{s}^{-3}$). Solid vertical lines indicate the location of the AEJ maximum. Dashed vertical line indicates the location of the maximum SMD concentration.
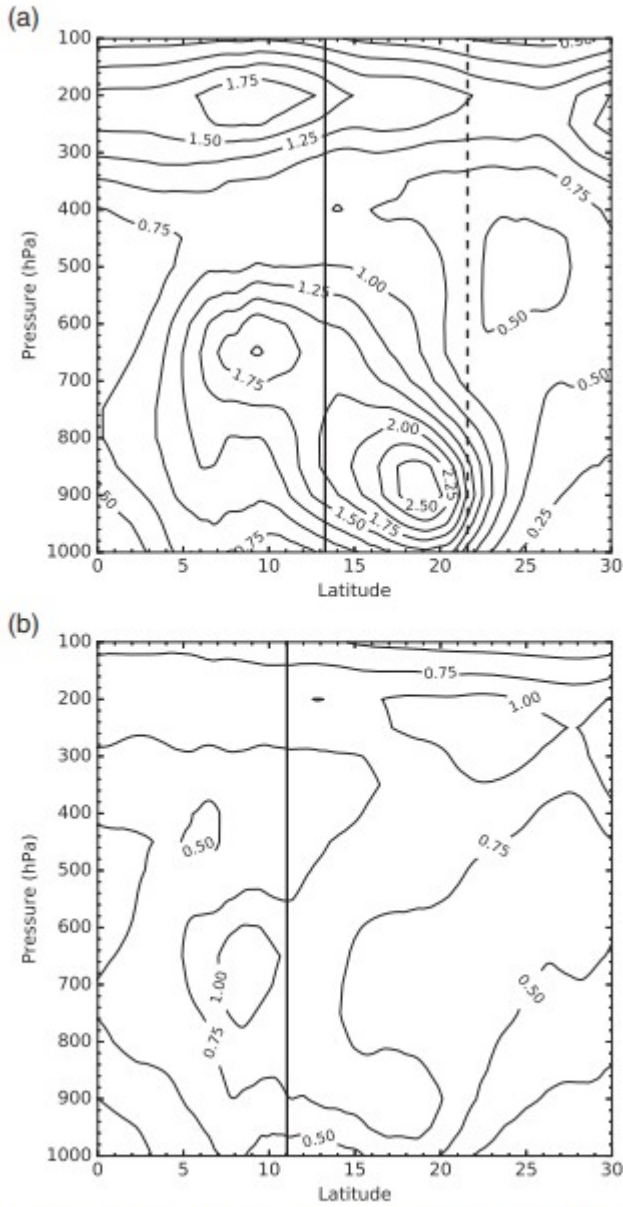
Figure 11. Barotropic energy conversion distribution, C_k^*, averaged between 30°W and 0° for (a) DUST-ON and (b) DUST-OFF (units: $10^{-4}\,\text{m}^2\,\text{s}^{-3}$). Solid vertical lines indicate the location of the AEJ maximum. Dashed vertical line indicates the location of the maximum SMD concentration.

Figure 12. Eddy kinetic energy distribution, K_E^*, averaged between 30°W and 0° for (a) DUST-ON and (b) DUST-OFF (units: $m^2 s^{-2}$). Solid vertical lines indicate the location of the AEJ maximum. Dashed vertical line indicates the location of the maximum SMD concentration.

Grogan *et al.* (2016) showed, based on their idealized WRF-dust model, that G_E^* is due to SMD-modified baroclinic effects and SMD-modified eddy APE. Their equation for G_E^* can, after rearrangement of terms, be written in the following symbolic form:

$$G_E^* = A\frac{\partial\overline{\gamma}}{\partial y} + B\frac{\partial\overline{\gamma}}{\partial p},$$

(3)

where $\bar{\gamma}$ is the dust mass mixing ratio and *A* and *B* are functions of the background wind, SMD, transmissivity, and eddy fluxes. Grogan *et al.* (2016) showed that G_E^* is maximized where the spatial gradients of SMD are maximized (in their study the meridional gradient term dominated). We obtain similar results: with SMD (Figure 9(a)), the maximum in G_E^* is 1.6 × 10^{-5} m² s⁻³ and is located near ~18°N, which approximately coincides with the maximum in the meridional SMD gradient (Figure 2). Without SMD (Figure 9(b)), the maximum in G_E^* is ~65% less and is ~250 hPa higher in altitude, which is outside of the region of the SMD plume. The horizontal and vertical spatial extent of G_E^*, which we measure by the positive contour G_E^* = 0.4 × 10^{-5} m² s⁻³, occupies ~8° latitude and ~300 hPa altitude with SMD, and ~3° latitude and ~100 hPa altitude without SMD.

Figure 10 shows the distribution of the baroclinic energy conversion, C_{pk}^*. Consistent with previous studies (Reed *et al.*, 1988; Hsieh and Cook, 2007), C_{pk}^* > 0 north of the AEJ near 800 hPa. With SMD, the maximum in C_{pk}^* is ~2.5° farther north, ~50% larger, and, in agreement with Grogan *et al.* (2016), coincides with the region where G_E^* and the meridional SMD gradient are also maximized. The northward shift in C_{pk}^* with SMD corresponds to the northward shift of the SMD-modified AEJ shown in Figure 5. Based on the C_{pk}^* = 0.2 × 10^{-4} m² s⁻³ contour, C_{pk}^* extends ~6° latitude and ~300 hPa with SMD (Figure 10(a)), and only ~1° latitude and ~150 hPa without SMD (Figure 10(b)). The effect of the SMD on C_{pk}^* is expected given that G_E^*, which is partially due to baroclinic effects, significantly increased with SMD and was maximized north of the AEJ.

Figure 11 shows the distribution of the barotropic energy conversion, C_k^*. With and without SMD, the (positive) first term on the right-hand side of Eq. 2c dominates. For both experiments, C_k^* is maximized south of the AEJ near 750 hPa, which is consistent with previous energetics analyses (Pytharoulis and Thorncroft, 1999; Kiladis *et al.*, 2006). The maximum C_k^* is ~115% larger with SMD, indicating greater energy transfer from the AEJ to the AEWs. Based on the C_k^* = 0.06 × 10^{-4} m² s⁻³ contour, C_k^* spans ~5° latitude and ~450 hPa with SMD, and ~2° latitude and ~350 hPa without SMD. The greater vertical and horizontal extent of C_k^* is due to the vertical and horizontal extension of the AEJ by the SMD. The SMD-induced changes to C_k^* increase the conversion of zonal kinetic energy to EKE.

Figure 12 shows the distribution of EKE, K_E^*. As in Hsieh and Cook (2007), regions of maximum K_E^* are north of the AEJ at ~900 hPa and south of the AEJ at ~700 hPa in both experiments. The regions of large K_E^* correspond to the northern and southern tracks of the AEWs (Figure 8), which are centred at 18.5°N and 9.5°N with SMD and 17.5°N and 8.5°N without SMD. With

SMD, the maximum K_E^* is ~3.2 m² s⁻² at 18.5°N, the latitude where the meridional SMD gradient is maximized. In contrast, without SMD, the maximum K_E^* is ~1.3 m² s⁻² at 8.5°N. The location of the maximum SMD-modified K_E^* coincides with the SMD-modified G_E^* and C_{pk}^* (Figures 9 and 10), both of which contribute to K_E^*. The maximum K_E^* for both tracks is on average ~150% larger with SMD. This is expected since the SMD increases the baroclinic and barotropic energy conversions.

6 SMD-modified pathways

To understand the quantitative results presented in the previous sections, we show in Figure 13 a scenario for communicating the effects of SMD to the AEJ-AEW system. Figure 13 highlights SMD-modified wave–mean flow interaction, though it is important to realize that other processes such as convection, which we do not consider in this figure, would also operate on the system. The scenario shown in Figure 13 pivots on the mobilization of SMD from its major sources regions, which are located north of the AEJ and near the northern track of the AEWs (Engelstaedter and Washington, 2007). The mobilization of SMD is due to several circulation features, which loft SMD into the lower atmosphere, where it is mixed vertically by boundary-layer processes and spread horizontally to form a synoptic-scale plume. The coarser SMD particles settle more quickly to the surface than the finer particles, which continue to be transported downstream by the AEJ and AEWs (Grogan et al., 2017). The radiative effects of SMD change both the mean and eddy portions of the heating field, which in turn affects the mean and eddy portions of the circulation. The two-way (nonlinear) interaction between the AEJ and the SMD is denoted by pathway 1. In a linear study, such as in Grogan et al. (2016), the background mean state is specified so that pathway 1 is fixed. The two-way (nonlinear) interaction between the northern track AEWs and the SMD is denoted by pathway 2. The SMD-modified wave–mean flow interaction is denoted by pathways A and B.
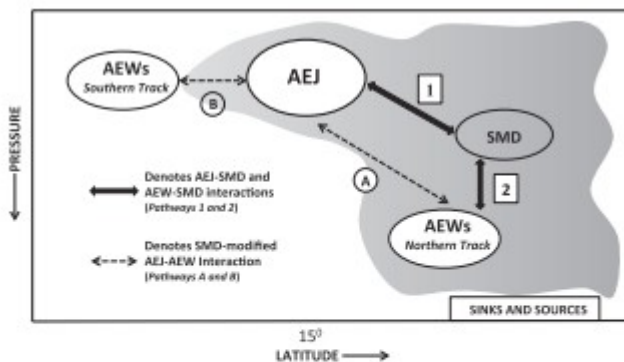

Figure 13. Schematic showing the key wave–mean flow interaction pathways that communicate the effects of SMD to the AEJ-AEW system (not drawn to scale). Thick arrows denote the two-way interactions between the SMD and AEJ (pathway 1), and the SMD and AEWs (pathway 2). The dashed arrows denote the SMD-modified AEJ-AEW interactions (pathways A and B). See text for additional details.

Along pathway 1, SMD modifies the mean heating rate and thus the mean temperature field (Figure 4(c)), which modifies the AEJ and the mean meridional circulation. For example, Figure 4(c) shows increased heating in the SMD-modified mean temperature field north of ~15°N and near ~700 hPa, which is associated with the northward and upward shift of the AEJ and a sharpening of the mean shear north the AEJ axis (Figures 5 and 6). The SMD-modified mean circulation, in turn, affects the transport of SMD, which contributes to the time and zonally averaged SMD distribution shown in Figure 2.

Along pathway 2, SMD modifies the eddy-heating rate. As shown in Grogan *et al*. (2016) and Nathan *et al*. (2017), the SMD eddy-heating rate depends not only on the SMD transmissivity, but also on the background (mean) spatial gradients of the SMD field (see Eq. 3). If the mean horizontal spatial gradients are strong, as they are near the northern AEW track (Figure 2), then the effect of the eddy-heating rate on the AEWs will also be strong there. This is borne out by the large SMD-induced increase in the eddy APE and energy conversions seen along the northern AEW track, and the much smaller values seen along the southern AEW track (see section 5 and Figures 9-12). The SMD-modified changes in the AEWs will, in turn, affect the eddy transport of the SMD field. The two-way interaction between AEWs and the eddy SMD fields is responsible for the SMD-enhanced linear instability found by Grogan *et al*. (2016) and the subcritical destabilization of AEWs found by Nathan *et al*. (2017).

In addition to pathways 1 and 2 noted above, the effects of SMD on the AEJ and AEWs are also communicated throughout the AEJ-AEW system by wave–mean flow interaction, denoted by pathways A and B in Figure 13. Specifically, SMD-induced changes to the strength and shearing of the AEJ can affect the energy conversions to the AEWs, while the SMD-induced changes to the AEWs can affect their eddy flux convergences and thus their feedback on the AEJ. The differences in the way that pathways 1 and 2 and pathways A and B operate on the AEJ-AEW system manifest in the responses of the northern and southern AEW tracks. Recall, the northern track is close to the SMD source regions; consequently, the SMD concentrations and spatial gradients are large there, yielding SMD-induced changes to the AEWs via both pathway 2 and pathway A. In contrast, the weaker spatial SMD gradients south of the AEJ result in reduced eddy heating effects, so that the changes to the southern track are primarily due to the SMD-modified wave–mean flow interaction. Because the AEWs are tethered to the AEJ via wave–mean flow interaction, it is the SMD-induced shift in the AEJ that is primarily responsible for shifting the southern track northward (Figure 8).

7 Conclusions

The African easterly jet–African easterly wave (AEJ-AEW) system is a prominent circulation feature over North Africa, affecting weather from the African coast and the eastern Atlantic Ocean to the Americas (Reed *et al*.,

1977; Landsea, 1993). Because the AEJ-AEW system has regional and far-reaching effects on weather, it is particularly important to understand the processes that affect its structure, location and energetics.

Synoptic-scale plumes of Saharan mineral dust (SMD) aerosols that form episodically over North Africa during summer are among the processes that can affect the AEJ-AEW system. Indeed, we have shown, using the WRF model coupled to an interactive dust model, that for the period spanning July–September 2006, the radiative effects of SMD can have significant effects on the AEJ-AEW system. These SMD effects include enhancement of the downstream expansion of the AEJ-AEW system, shifts in the location of the AEJ-AEW system, and increases in the energetics terms within the AEJ-AEW system.

The effects of SMD on the AEJ-AEW system are robust. For example, with SMD, the AEJ core and AEW wavelengths expand downstream by ~75% and ~15–20% respectively, compared to ~30% and ~10–15% without SMD. The SMD-modified AEJ core shifts ~3° north, ~9° west and ~50 hPa vertically, and the northern and southern SMD-modified AEW tracks shift north by ~2.0° and ~3.0°, respectively. The SMD generation of eddy APE increases by a factor of 2.7 and the location of its maximum coincides with the maximum meridional SMD gradient. The baroclinic energy conversion increases by a factor of 2.5 with SMD and its maximum also coincides with the largest meridional SMD gradient. The EKE and the barotropic energy conversion increase with SMD by factors of 1.5 and 22, respectively.

The effects of SMD on the AEJ-AEW system have implications for the precipitation patterns over West Africa and tropical cyclogenesis over the eastern Atlantic Ocean. For example, we have shown that SMD strengthens the AEWs and shifts their tracks north, changes that may be related to precipitation patterns over West Africa. For instance, using 40 years of reanalysis data, Nicholson and Grist (2003) found that there is feedback between precipitation and the AEJ. The rainy season affects the location of the AEJ, while the AEJ modifies the development and organization of precipitation through AEWs. Using reanalysis and observational data, Kiladis et al. (2006) found that AEWs favour new convection as they propagate along a zonally varying AEJ. Grist (2002) analysed 40 years of reanalysis data and found that during wet years, there were a larger number of AEWs with relatively strong amplitudes, which was attributed to an increase in horizontal shear. SMD has also been shown to affect West African precipitation (Lau et al., 2009). Using a global climate model and prescribed SMD aerosol forcing, Lau et al. (2009) found that SMD strengthens the monsoon and shifts it northward, which implies an increase and northward shift of rainfall over West Africa. In light of the above studies and our results, we would expect an increase in precipitation with SMD, a consequence of the SMD-induced northward shift of the AEJ-AEW system, strengthening of the AEWs, and SMD microphysical effects (not examined here). Based on some preliminary calculations, we have indeed found that the SMD affects

precipitation: the SMD increases total accumulated rainfall by ~10% and shifts the region of precipitation ~5° north.

The strength of AEWs and their track locations are also important for tropical cyclogenesis, since AEWs are known to serve as seedling disturbances for tropical cyclones (Avila and Pasch, 1992; Landsea, 1993). Because AEWs with larger amplitudes have been positively correlated with tropical cyclone activity (Thorncroft and Hodges, 2001), the SMD-induced strengthening of the AEWs found in this study could foster tropical cyclone development. In addition, the location of AEWs has been found to play a role in tropical cyclone development. For example, the southern AEW track, in particular, has been identified as the track primarily responsible for tropical storm development (Thorncroft and Hodges, 2001). The ~3.0° (~330 km) SMD-induced northward shift of the southern track found here – which is mostly due to SMD-modified wave–mean flow interaction (pathway B in Figure 13; see section 6) – corresponds to a significant change in where AEWs exit the African coast. Moreover, we have shown that SMD-induced changes to the AEJ-AEW system cause the AEWs to zonally expand and increase their westward propagation. The track shift and propagation change together would affect both the location and the timing of tropical cyclogenesis.

Although our results offer further clarity on the effects of SMD on the AEJ-AEW system, questions remain. For example, how does SMD affect the interannual variability of the AEJ-AEW system? Here we focused on a seasonal average for a specific year. How does the intraseasonal variability of the SMD-modified AEJ-AEW system compare to a seasonal average? And can SMD microphysics, which was not examined in this study, further affect the AEJ-AEW system beyond the significant effects found here?

References

Avila LA, Pasch RJ. 1992. Atlantic tropical systems of 1991. *Mon. Weather Rev.* 120: 2688– 2696. https://doi.org/10.1175/1520-0493(1992)120<2688:ATSO>2.0.CO;2.

Banks JR, Brindley HE, Flamant C, Garay MJ, Hsu NC, Kalashnikova OV, Klüser L, Sayer AM. 2013. Intercomparison of satellite dust retrieval products over the west African Sahara during the Fennec campaign in June 2011. *Remote Sensing Environ.* 136: 99– 116. https://doi.org/10.1016/j.rse.2013.05.003.

Burpee RW. 1972. The origin and structure of easterly waves in the lower troposphere of North Africa. *J. Atmos. Sci.* 29: 77– 90. https://doi.org/10.1175/1520-0469(1972)029<0077:TOASOE>2.0.CO;2.

Carlson TN. 1969a. Synoptic histories of three African disturbances that developed into Atlantic hurricanes. *Mon. Weather Rev.* 97: 256– 276. https://doi.org/10.1175/1520-0493(1969)097<0256:SHOTAD>2.3.CO;2.

Carlson TN. 1969b. Some remarks on African disturbances and their progress over the tropical Atlantic. *Mon. Weather Rev.* 97: 716– 726. https://doi.org/10.1175/1520-0493(1969)097<0716:SROADA>2.3.CO;2.

Chen SH, Dudhia J, Kain JS, Kindap T, Tan E. 2008. Development of the online MM5 tracer model and its applications to air pollution episodes in Istanbul, Turkey and Sahara dust transport. *J. Geophys. Res.* 113: D11203. https://doi.org/10.1029/2007JD009244.

Chen SH, Wang SH, Waylonis M. 2010. Modification of Saharan air layer and environmental shear over the eastern Atlantic Ocean by dust-radiation effects. *J. Geophys. Res.* 115: D21202. https://doi.org/10.1029/2010JD014158.

Chen SH, Liu YC, Nathan TR, Davis C, Torn R, Sowa N, Cheng CT, Chen JP. 2015. Modeling the effects of dust-radiative forcing on the movement of Hurricane *Helene* (2006). *Q. J. R. Meteorol. Soc.* 141: 2563– 2570. https://doi.org/10.1002/qj.2542.

Cheng CT, Wang WC, Chen JP. 2010. Simulation of the effects of increasing cloud condensation nuclei on mixed-phase clouds and precipitation of a front system. *Atmos. Res.* 96: 461– 476. https://doi.org/10.1016/j.atmosres.2010.02.005.

Cornforth RJ, Hoskins BJ, Thorncroft CD. 2009. The impact of moist processes on the African easterly jet–African easterly wave system. *Q. J. R. Meteorol. Soc.* 135: 894– 913. https://doi.org/10.1002/qj.414.

Engelstaedter S, Washington R. 2007. Atmospheric controls on the annual cycle of North African dust. *J. Geophys. Res.* 112: D03103. https://doi.org/10.1029/2006JD007195.

Engelstaedter S, Tegen I, Washington R. 2006. North African dust emissions and transport. *Earth Sci. Rev.* 79: 73– 100. https://doi.org/10.1016/j.earscirev.2006.06.004.

Fiedler S, Schepanski K, Heinold B, Knippertz P, Tegen I. 2013. Climatology of nocturnal low-level jets over North Africa and implications for modeling mineral dust emission. *J. Geophys. Res.* 118: 6100– 6121. https://doi.org/10.1002/jgrd.50394.

Frank NL. 1970. Atlantic tropical systems of 1969. *Mon. Weather Rev.* 98: 307– 314. https://doi.org/10.1175/1520-0493(1970)098<0307:ATSO>2.3.CO;2.

Grist JP. 2002. Easterly waves over Africa. Part I: The seasonal cycle and contrasts between wet and dry years. *Mon. Weather Rev.* 130: 197– 211. https://doi.org/10.1175/1520-0493(2002)130<0197:EWOAPI>2.0.CO;2.

Grogan DFP, Nathan TR, Chen SH. 2016. Effects of Saharan dust on the linear dynamics of African easterly waves. *J. Atmos. Sci.* 73: 891– 911. https://doi.org/10.1175/JAS-D-15-0143.1.

Grogan DFP, Nathan TR, Chen SH. 2017. Saharan dust and the nonlinear evolution of the African easterly jet–African easterly wave system. *J. Atmos. Sci.* 74: 27– 47. https://doi.org/10.1175/JAS-D-16-0118.1.

Hall NMJ, Kiladis GN, Thorncroft CD. 2006. Three-dimensional structure and dynamics of African easterly waves. Part II: Dynamical modes. *J. Atmos. Sci.* 63: 2231– 2245. https://doi.org/10.1175/JAS3742.1.

Hess M, Koepke P, Schult I. 1998. Optical properties of aerosols and clouds: The software package OPAC. *Bull. Am. Meteorol. Soc.* 79: 831– 844. https://doi.org/10.1175/1520-0477(1998)079<0831:OPOAAC>2.0.CO;2.

Hong SY, Pan HL. 1996. Nonlocal boundary layer vertical diffusion in a medium-range forecast model. *Mon. Weather Rev.* 124: 2322– 2339. https://doi.org/10.1175/1520-0493(1996)124<2322:NBLVDI>2.0.CO;2.

Hsieh JS, Cook KH. 2007. A study of the energetics of African easterly waves using a regional climate model. *J. Atmos. Sci.* 64: 421– 440. https://doi.org/10.1175/JAS3851.1.

Iacono MJ, Delamere JS, Mlawer EJ, Shephard MW, Clough SA, Collins WD. 2008. Radiative forcing by long-lived greenhouse gases: Calculations with the AER radiative transfer models. *J. Geophys. Res.* 113: D13103. https://doi.org/10.1029/2008JD009944.

Jones C, Mahowald NM, Luo C. 2004. Observational evidence of African desert dust intensification of easterly waves. *Geophys. Res. Lett.* 31: L17208. https://doi.org/10.1029/2004GL020107.

Jury MR, Santiago MJ. 2010. Composite analysis of dust impacts on African easterly waves in the Moderate Resolution Imaging Spectrometer era. *J. Geophys. Res.* 115: D16213. https://doi.org/10.1029/2009JD013612.

Kain JS. 2004. The Kain–Fritsch convective parameterization: An update. *J. Appl. Meteorol.* 43: 170– 181. https://doi.org/10.1175/1520-0450(2004)043<0170:TKCPAU>2.0.CO;2.

Karyampudi VM, Carlson TN. 1988. Analysis and numerical simulations of the Saharan air layer and its effect on easterly wave disturbances. *J. Atmos. Sci.* 45: 3102– 3136. https://doi.org/10.1175/1520-0469(1988)045<3102:AANSOT>2.0.CO;2.

Kiladis GN, Thorncroft CD, Hall NMJ. 2006. Three-dimensional structure and dynamics of African easterly waves. Part I: Observations. *J. Atmos. Sci.* 63: 2212– 2230. https://doi.org/10.1175/JAS3741.1.

Knippertz P, Todd MC. 2010. The central west Saharan dust hot spot and its relation to African easterly waves and extratropical disturbances. *J. Geophys. Res.* 115: D12117. https://doi.org/10.1029/2009JD012819.

Knippertz P, Todd MC. 2012. Mineral dust aerosols over the Sahara: Meteorological controls on emission and transport and implications for modeling. *Rev. Geophys.* 50: RG1007. https://doi.org/10.1029/2011RG000362.

Kocha C, Lafore JP, Tulet P, Seity Y. 2012. High-resolution simulation of a major West African dust-storm: Comparison with observations and investigation of dust impact. *Q. J. R. Meteorol. Soc.* 138: 455– 470. https://doi.org/10.1002/qj.927.

Landsea CW. 1993. A climatology of intense (or major) Atlantic hurricanes. *Mon. Weather Rev.* 121: 1703– 1713. https://doi.org/10.1175/1520-0493(1993)121<1703:ACOIMA>2.0.CO;2.

Lau KM, Kim KM, Sud YC, Walker GK. 2009. A GCM study of responses of the atmospheric water cycle of West Africa and the Atlantic to Saharan dust radiative forcing. *Ann. Geophys.* 27: 4023– 4027. https://doi.org/10.5194/angeo-27-4023-2009.

Ma PL, Zhang K, Shi JJ, Matsui T, Arking A. 2012. Direct radiative effect of mineral dust on the development of African easterly waves in late summer, 2003–07. *J. Appl. Meteorol. Climatol.* 51: 2090– 2104. https://doi.org/10.1175/JAMC-D-11-0215.1.

Nathan TR, Grogan DFP, Chen SH. 2017. Subcritical destabilization of African easterly waves by Saharan mineral dust. *J. Atmos. Sci.* 74: 1039– 1055. https://doi.org/10.1175/JAS-D-16-0247.1.

Nicholson SE, Grist JP. 2003. The seasonal evolution of the atmospheric circulation over West Africa and Equatorial Africa. *J. Clim.* 16: 1013– 1030. https://doi.org/10.1175/1520-0442(2003)016<1013:TSEOTA>2.0.CO;2.

Pedlosky J. 2003. *Waves in the Ocean and Atmosphere: Introduction to Wave Dynamics*. Springer-Verlag: Berlin and Heidelberg, Germany.

Pytharoulis I, Thorncroft CD. 1999. The low-level structure of African easterly waves in 1995. *Mon. Weather Rev.* 127: 2266– 2280. https://doi.org/10.1175/1520-0493(1999)127<2266:TLLSOA>2.0.CO;2.

Reale O, Lau WK, Kim KM, Brin E. 2009. Atlantic tropical cyclogenetic processes during SOP-3 NAMMA in the GEOS-5 global data assimilation and forecast system. *J. Atmos. Sci.* 66: 3563– 3578. https://doi.org/10.1175/2009JAS3123.1.

Reale O, Lau KM, da Silva A. 2011. Impact of interactive aerosol on the African easterly jet in the NASA GEOS-5 global forecasting system. *Weather and Forecasting* 26: 504– 519. https://doi.org/10.1175/WAF-D-10-05025.1.

Reed RJ, Norquist DC, Recker EE. 1977. The structure and properties of African wave disturbances as observed during phase III of GATE. *Mon. Weather Rev.* 105: 317– 333. https://doi.org/10.1175/1520-0493(1977)105<0317:TSAPOA>2.0.CO;2.

Reed RJ, Klinker E, Hollingsworth A. 1988. The structure and characteristics of African easterly wave disturbances as determined from the ECMWF operational analysis/forecast system. *Meteorol. Atmos. Phys.* 38: 22– 33. https://doi.org/10.1007/BF01029944.

Riehl H. 1954. *Tropical Meteorology*. McGraw-Hill: New York, NY.

Slingo A, Ackerman TP, Allan RP, Kassianov EI, McFarlane SA, Robinson GJ, Barnard JC, Miller MA, Harries JE, Russell JE, Dewitte S. 2006. Observations of the impact of a major Saharan dust storm on the atmospheric radiation balance. *Geophys. Res. Lett.* 33: L24817. https://doi.org/10.1029/2006GL027869.

Tanaka TY, Chiba M. 2006. A numerical study of the contributions of dust source regions to the global dust budget. *Global Planet. Change* 52: 88– 104. https://doi.org/10.1016/j.gloplacha.2006.02.002.

Tegen I, Fung I. 1994. Modeling of mineral dust in the atmosphere: Sources, transport, and optical thickness. *J. Geophys. Res.* 99: 22897– 22914. https://doi.org/10.1029/94JD01928.

Thorncroft CD, Blackburn M. 1999. Maintenance of the African easterly jet. *Q. J. R. Meteorol. Soc.* 125: 763– 786. https://doi.org/10.1002/qj.49712555502.

Thorncroft CD, Hodges K. 2001. African easterly wave variability and its relationship to Atlantic tropical cyclone activity. *J. Clim.* 14: 1166– 1179. https://doi.org/10.1175/1520-0442(2001)014<1166:AEWV AI>2.0.CO;2.

Tompkins AM, Cardinali C, Morcrette JJ, Rodwell M. 2005. Influence of aerosol climatology on forecasts of the African easterly jet. *Geophys. Res. Lett.* 32: L10801. https://doi.org/10.1029/2004GL022189.

Wilcox EM, Lau KM, Kim KM. 2010. A northward shift of the North Atlantic Ocean intertropical convergence zone in response to summertime Saharan dust outbreaks. *Geophys. Res. Lett.* 37: L04804. https://doi.org/10.1029/2009GL041774.

Wong S, Dessler AE, Mahowald NM, Yang P, Feng Q. 2009. Maintenance of lower tropospheric temperature inversion in the Saharan air layer by dust and dry anomaly. *J. Clim.* 22: 5149– 5162. https://doi.org/10.1175/2009JCLI2847.1.

Xie Y, Zhang Y, Xiong X, Qu JJ, Che H. 2011. Validation of MODIS aerosol optical depth product over China using CARSNET measurements. *Atmos. Environ.* 45: 5970– 5978. https://doi.org/10.1016/j.atmosenv.2011.08.002.

Zhu A, Ramanathan V, Li F, Kim D. 2007. Dust plumes over the Pacific, Indian, and Atlantic Oceans: Climatology and radiative impact. *J. Geophys. Res.* 112: D16208. https://doi.org/10.1029/2007JD008427.